I&EC research
Industrial & Engineering Chemistry Research
pubs.acs.org/IECR
Article

High-Capacity Regenerable H_2S Sorbent for Reducing Sulfur Emissions

Wenyang Zhao, Balasubramanian Veerappan Vaithilingam, Supriya Ghosh, Xinyu Li, Frank Geuzebroek, Adel Saif El Nasr, Ibrahim Khan, Satyadileep Dara, Nitish Mittal, Prodromos Daoutidis, Saleh Al Hashimi, K. Andre Mkhoyan,* Yasser Al Wahedi,* Michael Tsapatsis,* and Andreas Stein*

Cite This: *Ind. Eng. Chem. Res.* 2021, 60, 14779−14787

ABSTRACT: The separation of H_2S from natural gas, biogas, and coal gas is an essential process that requires large energy input and high capital costs. We propose a new sorption-based process, which can be coupled with the Claus desulfurization process to reduce sulfur emissions. This new process is based on a new sorbent material consisting of a specific composition of Cu, Mg, and Al oxides and exhibiting superior sulfur capacity (~7.5 mmol/g) at process conditions compatible for integration with the Claus process. CuO is the active sorbent component, which during H_2S uptake is converted to CuS and can be fully regenerated during cyclic operation. Al_2O_3 and small amounts of MgO are shown to be essential components that contribute to sorbent activity and stability.

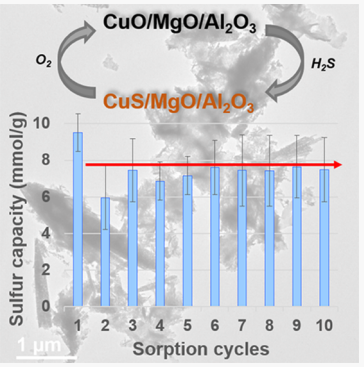

1. INTRODUCTION

H_2S is a common contaminant of natural gas, biogas, and coal gas, and is highly poisonous, corrosive, and flammable.[1−3] It causes detrimental effects to gas liquefaction and storage facilities due to pipeline corrosion, and it deactivates most industrial catalytic processes in which reduced metals are used as the primary active phase. During combustion, H_2S is converted to sulfur oxides (SO_x), which are the principal contributors to acid rain, damaging ecosystems and impacting human health. It is therefore critical to remove H_2S to meet both gas market standards and environmental regulations.

Amine gas treatment is the primary process of sulfur recovery units (SRUs), which use aqueous solutions of alkylamines to capture H_2S.[4−6] Amines, as well as other processes, are employed in tail-gas treatment units (TGTUs) for H_2S elimination from the widely used Claus process.[7,8] A simulation study indicated that using a regenerable sorbent capable of adsorbing H_2S from Claus tail gas at moderate temperatures (ca. 150 °C) in a temperature swing adsorption-based process offers capital cost and energy efficiency benefits compared to commercial amine TGTUs.[9] However, the preparation of a sorbent with appropriate capacity and sufficient stability upon regeneration has not been achieved.[1,10−13] We therefore decided to explore the possible use of solid regenerable sorbents in place of porous sorbents.

While various metal oxide-based sorbents have been developed, including ZnO, CuO, Cr_2O_3, Fe_2O_3, Mn_2O_3, and others,[1,14−19] most are limited by low utilization (especially at low temperatures) and/or incomplete regeneration during cycling between the sulfide and the oxide phases, resulting in low effective sulfur capacity.

In the present study of CuO-based solid sorbents prepared by a precipitation method, a mixed metal oxide (MMO) sorbent composition that is highly effective for gas desulfurization at low concentrations of H_2S is identified. With optimized amounts of MgO and Al_2O_3 additives, the sorbent exhibits superior sulfur capacity and stability over repetitive sulfidation−regeneration cycling. H_2S sorption can be accomplished at 150 °C, allowing for energy-efficient process integration with the Claus process.

2. EXPERIMENTAL SECTION

2.1. Materials. The chemicals used in this study were obtained from the following sources: copper(II) nitrate trihydrate (ACS reagent, ≥99%), magnesium nitrate hexahydrate (ACS reagent, ≥98%), aluminum nitrate nonahydrate (ACS reagent, ≥98%), molecular sieves (3 Å) from Sigma-Aldrich; sodium carbonate anhydrous (powder/certified ACS) from Fisher Chemical; quartz wool (fine, 4 μm) from Acros Organics; N_2, CO_2, and 100 ppmv H_2S in N_2 from Matheson;

Received: July 9, 2021
Revised: September 10, 2021
Accepted: September 13, 2021
Published: September 23, 2021

and 5% O_2 in N_2 from Praxair. Deionized water was purified to a minimum resistivity of 18.2 MΩ·cm with a Milli-Q PLUS reagent-grade water system and was used in all experiments.

2.2. Synthesis of the Solid Sorbent. Three separately prepared solutions of 1.25 M $Cu(NO_3)_2$, 1.25 M $Mg(NO_3)_2$, and 1.25 M $Al(NO_3)_3$ were mixed together in a beaker. A plastic syringe was loaded with this mixed nitrate solution. A separate 500 mL polypropylene bottle was filled with 100 mL of deionized water and heated in an oil bath at 70 °C with vigorous magnetic stirring. The mixed metal nitrate solution was added to the polypropylene bottle at a rate of 5 mL/min using a syringe infusion pump. The pH of the entire reaction mixture was maintained at a value of 7 by manual in situ addition of a 1.25 M Na_2CO_3 solution. Upon complete addition of the mixed metal nitrate solution, the reaction temperature was increased to 80 °C and kept there for 1 h under continuous stirring to age the mixture. The resulting precipitate was filtered and washed 3 times, each time with 2 L deionized water. The material was dried at 70 °C for 12 h and then calcined at 500 °C for 5 h in air flowing at a rate of ∼100 mL/min. The final material was denoted as 6:3:1 based on the volume ratio between the Cu, Mg, and Al nitrate solutions. Similarly, 1:0:0 indicates that the starting nitrate solution consisted of 50 mL of 1.25 M $Cu(NO_3)_2$ only, while 6:3:0 indicates that the starting nitrate solution contained 33.3 mL of 1.25 M $Cu(NO_3)_2$ and 16.7 mL of 1.25 $Mg(NO_3)_2$, etc. The metal nitrate solution volumes for all of the samples are summarized in Table 1.

Table 1. Samples Prepared from Mixed Nitrate Solutions with Different Compositions

sample names	volume of 1.25 M $Cu(NO_3)_2$ (mL)	volume of 1.25 M $Mg(NO_3)_2$ (mL)	volume of 1.25 M $Al(NO_3)_3$ (mL)
1:0:0	50.0	0	0
6:3:0	33.3	16.7	0
6:0:1	42.9	0	7.1
5:3:1	27.8	16.7	5.5
6:3:1	30.0	15.0	5.0
6.5:3:1	31.0	14.3	4.7

2.3. H_2S Sorption. The experimental setup for sulfidation−regeneration studies was constructed from stainless steel 316 tubing and connections. A mass of 5.0 mg of the sorbent (mesh 40−80) was diluted with 100.0 mg of quartz (mesh 40−80) and sandwiched between quartz wool plugs in a U-shaped quartz tube with a 4 mm inner diameter. At the downstream end of the quartz tube, a ∼200 mg molecular sieve (3 Å) (mesh 40−80) was packed in the tubing to remove water from the system. The sorbent was activated in a 40 mL/min N_2 flow at 300 °C for 12 h and then exposed to a H_2S stream of 40 mL/min (100 ppmv in N_2) at 150 °C and 1 atm. The H_2S concentration at the reactor exit was monitored using a gas chromatograph (Agilent 7890A) equipped with a sulfur chemiluminescence detector (SCD). The breakthrough capacity was determined at an exit H_2S concentration equal to 5% of the inlet concentration. The sulfidated sorbent was regenerated by oxidation in the same reactor at 600 °C for 6 h in 5% O_2 (balanced with N_2) flowing at a rate of 40 mL/min. The reactor was flushed with N_2 for at least 15 min between cycles as a safety precaution. The flow rates were calibrated using a soap film flowmeter. For sorbent 6:3:1, H_2S sorption experiments were also carried out at 200, 250, and 300 °C, and regeneration was also performed at 550 °C.

H_2S sorption was also carried out at Alberta Sulphur Research Ltd. using simulated gas with a flow rate of 42 mL/min. The composition of the simulated gas was H_2S, 1435 ppmv; H_2, 2.47%; H_2O, 30.89%; CO, 0.0098%; CO_2, 17.37%; and N_2, 49.12%. In this case, 25 mg of the sorbent was diluted with 500 mg of quartz in the sorption bed. The sorbent was activated in a 40 mL/min N_2 flow at 300 °C for 12 h and then exposed to the simulated gas at 150 °C and 1 atm.

2.4. Characterization. Powder X-ray diffraction (XRD) patterns of the materials were obtained using a PANalytical X'Pert Pro diffractometer outfitted with an X'Celerator detector and a Co anode (Kα radiation, λ = 1.789 Å) operated at 45 kV and 40 mA. Scanning electron microscopy (SEM) was performed on a JEOL-6500 field emission scanning electron microscope with an accelerating voltage of 5.0 kV. All samples were coated with a 50 Å platinum film prior to SEM imaging. Nitrogen sorption experiments were performed on a Quantachrome Autosorb-iQ_2 analyzer. All samples were degassed under dynamic vacuum (∼0.003 mTorr) at 120 °C for 12 h before analysis. Brunauer−Emmett−Teller (BET) surface areas were evaluated from the adsorption isotherms in the relative pressure range of 0.05−0.35. Conventional transmission electron microscopy (TEM) images were obtained using an FEI Tecnai T12 TEM with a LaB_6 filament at an accelerating voltage of 120 kV. High-resolution transmission electron microscopy (HRTEM) images were taken using an FEI Tecnai G2 F30 field emission gun transmission electron microscope with an accelerating voltage of 300 kV. TEM samples were prepared by dispersing the materials on carbon-coated Cu or Mo grids. High-angle annular dark-field scanning transmission electron microscopy (HAADF-STEM) imaging was performed at 200 kV with an incident semiconvergent angle of 25.5 mrad and detector collection angles of 58.5−200 mrad on an aberration-corrected FEI Titan G2 60-300 STEM. The electron probe was corrected using a CEOS-DCOR probe corrector to achieve 0.8 Å imaging resolution. Energy-dispersive X-ray (EDX) spectral imaging was performed by STEM using a Super-X system at 200 and 80 kV and a 20−30 pA beam current. Elemental analyses were performed by the Microanalysis Lab at the University of Illinois at Urbana-Champaign and by Galbraith Laboratories, Inc. The metal content was measured using inductively coupled plasma atomic emission spectroscopy (ICP-AES) using Optima 8300 and Optima 5300 Analyzers. Samples were digested with HNO_3 at room temperature and analyzed for Cu, Mg, and Al contents.

3. RESULTS AND DISCUSSION

3.1. Reactive H_2S Sorption of CuO. The sorbent materials are intended for a sorption−regeneration process (SRP) for H_2S separation. One complete SRP cycle includes reactive H_2S sorption at 150 °C and oxidative desorption at 600 °C. The latter was selected based on the decomposition temperature of CuS. CuO converts to CuS during H_2S sorption (Reaction 1). Alternatively, H_2S can act as a reducing agent and be oxidized by CuO, forming Cu_2S and SO_2 (Reaction 2).[20−22] This reaction is undesirable and should be minimized because it lowers sorbent efficiency, as two moles of CuO capture only one mole of H_2S. In addition, the released SO_2 can break through the bed. We therefore set an upper limit of 5% SO_2 in the bed effluent during sorption as an

https://doi.org/10.1021/acs.iecr.1c02715
Ind. Eng. Chem. Res. 2021, 60, 14779−14787

Table 2. H_2S Sorption Capacity for Sorbents Prepared from Precursors with the Indicated Nominal Cu, Mg, and Al Molar Ratios

sample names	molar ratio of Cu/Mg/Al[a]			chemical formula	theoretical capacity[b] (mmol/g)	summary of performance testing
1:0:0	N/A	N/A	N/A	CuO	12.6	first cycle 8.2 mmol/g, second cycle 4.9 mmol/g, more than 5% SO_2 detected during the first sulfidation
6:3:0	50	1	N/A	$Cu_{50}MgO_{51}$	12.4	first cycle 8.5 mmol/g, second cycle 6.0 mmol/g, more than 5% SO_2 detected during the second sulfidation
6:0:1	6.2	N/A	1	$Cu_{6.2}AlO_{7.7}$	11.4	first cycle 7.1 mmol/g, ∼30% SO_2 detected during the second sulfidation
6.5:3:1	6.9	0.41	1	$Cu_{6.9}Mg_{0.41}AlO_{8.8}$	11.2	first cycle 8.0 mmol/g, second cycle 3.5 mmol/g, third cycle 4.5 mmol/g, fourth cycle 3.9 mmol/g, fifth cycle 4.0 mmol/g
6:3:1	6.2	0.21	1	$Cu_{6.2}Mg_{0.21}AlO_{7.9}$	11.2	first cycle 9.5 mmol/g, second cycle 6.0 mmol/g, third cycle 7.5 mmol/g, fourth cycle 6.9 mmol/g, fifth cycle 7.2 mmol/g, then remaining stable ∼7.5 mmol/g for another five cycles
5:3:1	5.3	0.47	1	$Cu_{5.3}Mg_{0.47}AlO_{6.9}$	10.8	first cycle 6.6 mmol/g, second cycle 3.2 mmol/g, third cycle 4.0 mmol/g, fourth cycle 3.9 mmol/g

[a]Determined by ICP-AES elemental analysis. [b]Calculated assuming all of the CuO can react with H_2S with a 1:1 stoichiometry.

additional criterion for evaluating sorbent performance. If more than 5% SO_2 is detected during H_2S sorption, we consider the material unsuitable for long-term operation. Once the sorption process ends, the gas stream is switched to 5% O_2/N_2, under which CuS converts back to CuO. During regeneration, a series of reactions occurs, in which CuS is oxidized to $CuSO_4$ and $CuO{\cdot}CuSO_4$ before complete decomposition to CuO.[23] Dunn et al. reported in detail on the thermal oxidation of CuS by heating covellite in air, concluding that a typical reaction path follows the sequence $CuS \rightarrow Cu_2S \rightarrow CuSO_4 \rightarrow CuO{\cdot}CuSO_4 \rightarrow CuO$, where decomposition of $CuO{\cdot}CuSO_4$ occurs at 653 °C.[23] Reaction 3 represents the simplified overall reaction.

$$CuO + H_2S \rightarrow CuS + H_2O \quad (1)$$

$$6CuO + 4H_2S \rightarrow 3Cu_2S + SO_2 + 4H_2O \quad (2)$$

$$CuS + 1.5O_2 \rightarrow CuO + SO_2 \quad (3)$$

Pure CuO (here denoted as sorbent 1:0:0 according to the molar composition ratio of the Cu/Mg/Al nitrate precursor) had a high initial sulfur capacity of 8.2 mmol/g but produced more than 5% SO_2 before the breakthrough of H_2S during the first sulfidation, which suggests a significant contribution from the undesirable Reaction 2 (Figure S1). This was further confirmed by the X-ray diffraction (XRD) pattern of 1:0:0 (CuO) after the first sulfidation, in which both CuS and Cu_2S were detected (Figure S2). Because the H_2S breakthrough curve leveled off during the first sulfidation, indicating that sorption was complete, we confirmed that the Cu_2S present in the material obtained at the end of the breakthrough could not react any further with H_2S under the current conditions. The total amount of SO_2 generated during the first sulfidation was 1.0 mmol/g. Oxidation of H_2S to SO_2 on a CuO surface was reported earlier, and the concentration of SO_2 was found to increase with increasing sulfidation temperature.[22,24] Besides this side reaction, pure CuO could not retain its capacity after regeneration. As calculated from the breakthrough curve in Figure S1, the sulfur capacity during the second sulfidation dropped to 4.9 mmol/g, a ∼40% decrease compared to that of the fresh sorbent.

3.2. Influence of MgO as an Additive to the Sorbent Material. Density functional theory studies[25,26] suggested that basic sites from MgO can facilitate adsorption and dissociation of H_2S, potentially enhancing the sorbent's overall sorption ability. With motivation from these theoretical works, an MMO containing CuO and MgO was prepared through coprecipitation, aiming to avoid the capacity loss of CuO after regeneration. Table 2 includes the actual composition of MMOs determined by inductively coupled plasma atomic emission spectroscopy (ICP-AES) and the theoretical sulfur capacity, which was calculated assuming that all of the CuO in the sorbent reacts with H_2S following Reaction 1. Elemental analyses indicate that sorbent compositions are far from the nitrate solution compositions given in Table 1 because the majority of the Mg^{2+} species cannot precipitate during the synthesis at pH 7, which agrees with results reported by Wang et al. and Seron et al.[27,28]

Sorbent 6:3:0 was prepared using a 6:3 ratio of 1.25 M $Cu(NO_3)_2$ and 1.25 M $Mg(NO_3)_2$ solutions, as described in Table 1. Its composition, determined by ICP-AES, yields the chemical formula $Cu_{50}MgO_{51}$, as listed in Table 2. Sorbent 6:3:0 ($Cu_{50}MgO_{51}$) performed well during the first sulfidation (breakthrough capacity 8.5 mmol/g) without exceeding the SO_2 limit in the effluent; however, more than 10% SO_2 was formed, and the sulfur capacity dropped by ∼30% in the second cycle (Figures S3), suggesting that during the second sulfidation, much less CuO was active compared to the fresh sorbent. The cause for increased SO_2 formation during the second sulfidation was revealed by the XRD pattern of this sorbent after the first regeneration. As shown in Figure S4, in addition to CuO, a $CuO{\cdot}CuSO_4$ phase was now present, originating from a solid solution of CuO and $CuSO_4$ formed during oxidation of CuS. This indicates that 6:3:0 ($Cu_{50}MgO_{51}$) cannot be fully regenerated. For a separately prepared crystalline $CuO{\cdot}CuSO_4$ sample (Figure S5), during H_2S sorption more than 30% SO_2 was detected in the effluent (Figure S6). This indicates that if the sorbent is not fully regenerated, any residual $CuO{\cdot}CuSO_4$ oxidizes H_2S to SO_2 in the next sorption cycle, leading to undesired early sulfur breakthrough.

With MgO present in the sorbent, a potential problem is the formation of $MgSO_4$ after regeneration, which may affect the sorption performance in the following cycles. During the thermal oxidation of CuS, the last step is the decomposition of $CuO{\cdot}CuSO_4$, which releases SO_3 (Reaction 4).[23] MgO can react with SO_3 because of its basic surface and form $MgSO_4$ (Reaction 5).[29,30] The decomposition temperature of $MgSO_4$ is higher than 1000 °C, and thus MgO cannot be fully regenerated at 600 °C if Reaction 5 occurs.[31]

https://doi.org/10.1021/acs.iecr.1c02715
Ind. Eng. Chem. Res. 2021, 60, 14779−14787

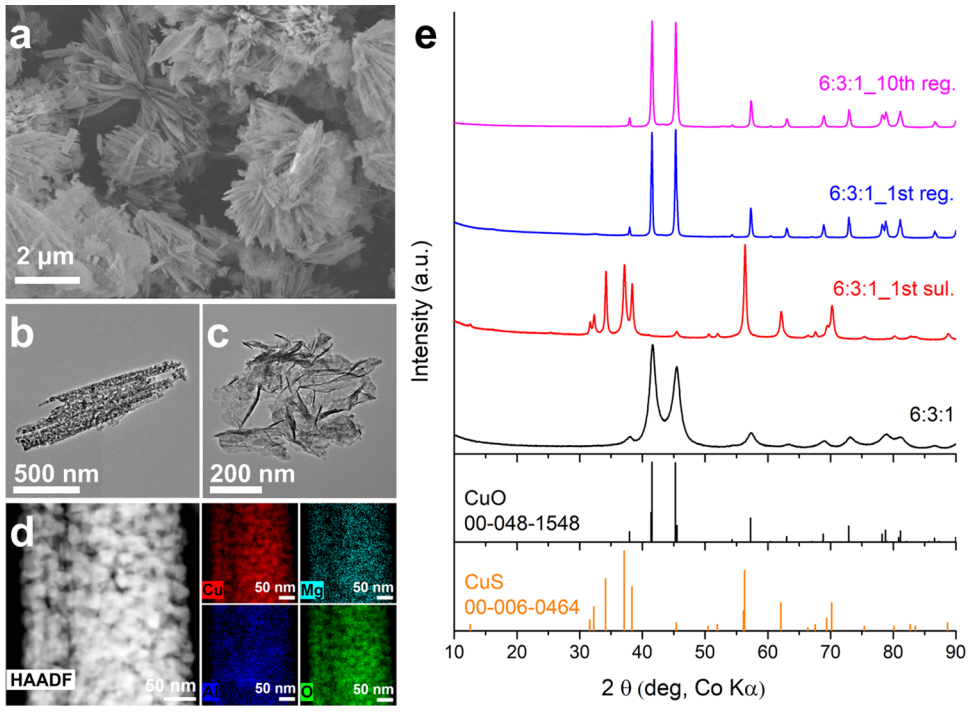

Figure 1. Microstructural characterization of the as-made, high-performance sorbent 6:3:1 ($Cu_{6.2}Mg_{0.21}AlO_{7.9}$). (a) SEM and (b, c) TEM images, in which both nanorod (b) and nanosheet morphologies (c) can be observed. (d) High-angle annular dark-field (HAADF)-STEM image of 6:3:1 ($Cu_{6.2}Mg_{0.21}AlO_{7.9}$) with corresponding STEM-EDX elemental maps. (e) XRD patterns of the sorbent 6:3:1 ($Cu_{6.2}Mg_{0.21}AlO_{7.9}$) as made, after the first sulfidation step, after the first regeneration step, and after 10 sulfidation−regeneration cycles.

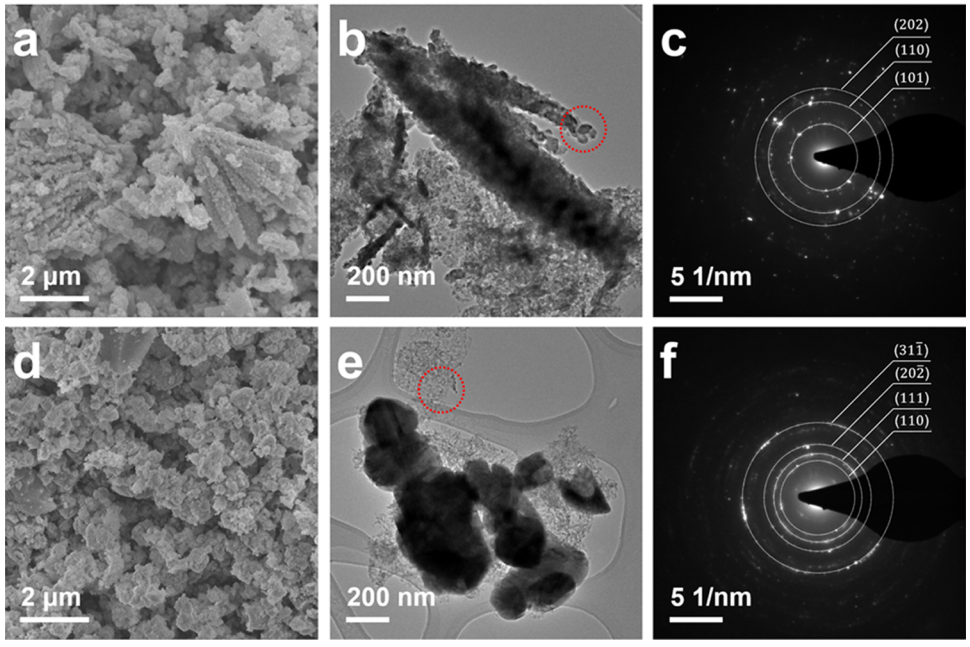

Figure 2. Morphological changes after sulfidation and regeneration. (a, b) SEM and TEM images of 6:3:1 ($Cu_{6.2}Mg_{0.21}AlO_{7.9}$) after the first sulfidation step and (d, e) after the first regeneration step. (c, f) SAED patterns collected from the regions indicated by red circles in (b, e); the indexed circles in (c, f) indicate the corresponding diffractions of CuS and CuO, respectively.

$$CuO{\cdot}CuSO_4 \rightarrow 2CuO + SO_3 \quad (4)$$

$$MgO + SO_3 \rightarrow MgSO_4 \quad (5)$$

3.3. Influence of Combined MgO and Al_2O_3 Additives. Considering the possible formation of $MgSO_4$, we first tested sorbent 6:0:1 ($Cu_{6.2}AlO_{7.7}$) without MgO. The capacity was 7.1 mmol/g in the first cycle, and SO_2 topped 5%. After regeneration, SO_2 reached 30% in the second cycle, far exceeding the 5% upper limit of SO_2 in the effluent (Figure S7). We further incorporated Al_2O_3 into CuO/MgO, a material commonly used to increase the stability of catalysts and sorbents, as a means to disperse MgO species. Sorbent 6.5:3:1 ($Cu_{6.9}Mg_{0.41}AlO_{8.8}$) exhibited a high initial capacity of 8.0 mmol/g (Figures S8 and S9). After the first regeneration,

https://doi.org/10.1021/acs.iecr.1c02715
Ind. Eng. Chem. Res. 2021, 60, 14779−14787

however, a 56% drop in capacity was observed for the second sulfidation. The capacity increased slightly during the following cycles and stabilized at ~4 mmol/g in five cycles. A similar trend was observed for sorbent 5:3:1 ($Cu_{5.3}Mg_{0.47}AlO_{6.9}$), with a 52% capacity drop from cycle 1 to cycle 2 before stabilizing at ~4 mmol/g in four cycles (Figures S10 and S11). Importantly, SO_2 was not detected at high levels throughout, which confirms that $CuO{\cdot}CuSO_4$ in both sorbents was fully decomposed during regeneration.

In the case of sorbent 6:3:1 ($Cu_{6.2}Mg_{0.21}AlO_{7.9}$), a drop from 9.5 to 6.0 mmol/g occurred from cycle 1 to cycle 2, but the capacity later increased and stabilized at 7.5 mmol/g, and only a negligible amount of SO_2 was generated during each cycle (Figures S12 and S13). To the best of our knowledge, this is the highest sulfur capacity reported for any metal oxide-based regenerable sorbent that works at relatively low (<300 °C) temperatures (Table S1). To gain a better understanding of the high-performing sorbent 6:3:1 ($Cu_{6.2}Mg_{0.21}AlO_{7.9}$), we characterized this sorbent in more detail.

3.4. Cycling Behavior of Sorbent 6:3:1 ($Cu_{6.2}Mg_{0.21}AlO_{7.9}$). Sorbent 6:3:1 ($Cu_{6.2}Mg_{0.21}AlO_{7.9}$) contains crystalline CuO with a grain size of 14 nm calculated from XRD line broadening (Figure 1e), which agrees with grain sizes observed in the TEM dark-field image (Figure S14). While the MgO content is below the detection limit of XRD, the XRD pattern did not reveal any crystalline Al_2O_3. SEM images show a predominant nanorod morphology (Figure 1a), whereas co-existing nanorods and nanosheets are seen by TEM (Figures 1b,c and S15). Both nanorod and nanosheet structures contain crystalline CuO (Figure S16). The periodicity of the CuO lattice fringes observed in fast-Fourier transforms of the images demonstrates the alignment of the CuO grains in the nanorods (Figure S17). In contrast, the CuO grains are randomly oriented in the nanosheets (Figure S18). Elemental mapping indicates that Cu, Mg, and Al species are uniformly distributed at ca. 10 nm scale (Figure 1d).

Reactive sorption and regeneration cause structural and morphological changes in sorbent 6:3:1 ($Cu_{6.2}Mg_{0.21}AlO_{7.9}$). As shown in Figure S19d–f, most of the grains in the sorbent particles grew in size after the first sulfidation, while the nanorod morphology can still be seen (Figure 2a). Compared to the nanorods in the fresh sorbent, these particles are bulkier and have a rougher surface, implying grain growth during sulfidation. A considerable volume increase is inevitable during transformation from CuO to CuS, as CuS (20.1 cm^3/mol) is 60% larger than CuO (12.6 cm^3/mol) in terms of molar density. A nitrogen sorption isotherm (Figure S20) indicates that the sorbent contains mainly mesopores and macropores with a BET surface area of 52 m^2/g. The TEM image in Figure 2b and the associated electron diffraction pattern in Figure 2c indicate the formation of CuS. Diffraction analysis of a partially sulfidated sample reveals that at the early stages of H_2S sorption, CuS is uniformly distributed in the fraction of the sorbent with small grains, less than 5 nm in size (Figures S21 and S22). After complete sulfidation, the grains grow much larger, with an average CuS grain size of 65 nm. As shown by the XRD data in Figure 1e, CuS is the only crystalline phase in the sulfidated sorbent, and Cu_2S is not formed.

After full sulfidation at 150 °C, as confirmed by the leveling off of the breakthrough curve, regeneration was carried out at 600 °C in 5% O_2/N_2 for 6 h. As shown in Figure 2d,e, after the first sulfidation–regeneration cycle, the original morphology changes drastically to one of particle aggregates. Crystalline CuO was observed by electron diffraction, as shown in Figure 2f.

The XRD patterns of 6:3:1 ($Cu_{6.2}Mg_{0.21}AlO_{7.9}$) at different stages are shown in Figure 1e, and the estimated crystallite sizes of CuO are summarized in Table S2. In the fresh sorbent, crystalline CuO has an average size of 14 nm. The CuO reacted with H_2S with a 1:1 stoichiometry during sulfidation and formed CuS. After regeneration, only CuO appeared in the XRD pattern, with no evidence of CuS, $CuSO_4$, nor $CuO{\cdot}CuSO_4$. CuO grains grew to 93 nm and remained smaller than 100 nm after 10 cycles (Table S2), with stable sulfur capacities throughout. On the other hand, when regeneration was carried out at 550 °C, other sulfate species appeared in the XRD pattern (Figure S24). The morphological changes mainly occurred during the first regeneration. As shown in Figures 2e and S25, the morphology of 6:3:1 ($Cu_{6.2}Mg_{0.21}AlO_{7.9}$) was similar after the first and tenth regeneration steps; in both cases, the sorbent contained particles with sizes larger than 100 nm and aggregates of nanoparticles with grain size less than 50 nm. It appears that sorbent sintering occurred mainly during the first regeneration, which explains the capacity drop from 9.5 to 6.0 mmol/g from cycle 1 to cycle 2.

3.5. Process-Scale Assessment. To assess the economic competitiveness of sorbent 6:3:1 ($Cu_{6.2}Mg_{0.21}AlO_{7.9}$), we conducted a simulation study of a SRP-based system and compared it to the Shell Claus Off-gas Treating (SCOT) process, following the same approach used previously for a sorbent based on Cu-exchanged zeolite Y.[9,32] As discussed in Section S5, the SRP and SCOT technologies are compared as retrofit options to a brownfield gas processing facility. Specifically, the two technologies are evaluated as options to be inserted into the red box in the natural gas processing value chain shown in Figure S26, just after the SRU based on the Claus process. Details of the models, associated inputs, and assumptions are available in the Supporting Information.

As shown in Figure 3, similar to the SCOT process (Figure S27), the SRP system is designed for achieving maximum

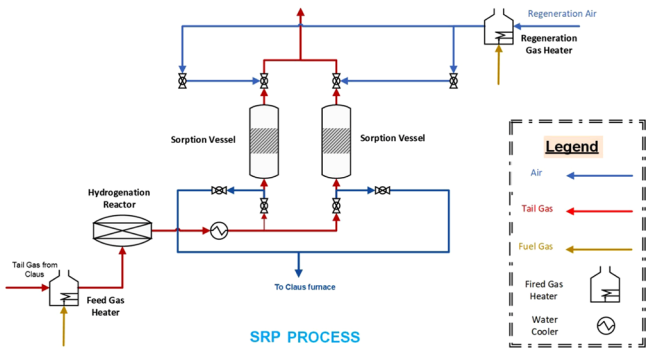

Figure 3. Schematic of the proposed SRP system.

sulfur conversion. Prior to the hydrogenation step, the Claus tail gas feed is first heated in a fired gas heater to 240 °C, the required temperature for hydrogenation of all sulfur species. Subsequently, the effluent gas is introduced to a typical hydrogenation reactor. The hydrogenation step targets the complete transformation of all sulfur species to H_2S in addition to a significant destruction of CO via the water gas shift reaction. A screening experiment indicated that at higher sulfidation temperatures, more SO_2 tends to be formed (Figure S28). The effluent of the reactor is therefore introduced to a

https://doi.org/10.1021/acs.iecr.1c02715
Ind. Eng. Chem. Res. 2021, 60, 14779–14787

water-based cooler to reduce the temperature to 150 °C. Once the breakthrough point of H_2S is reached, the Claus tail gas flow is switched to the standby vessel. During regeneration, a slipstream of the Claus unit air feed is rerouted using a centrifugal blower to a fired gas heater, where it is heated to 600 °C. The hot air stream is routed to the bed undergoing regeneration, and the bed is regenerated to fresh condition. Finally, the air stream effluent of the centrifugal blower is introduced to the vessel after complete regeneration for cooling to 150 °C, thus preparing for the next sorption cycle.

Solid sorbents have the advantage of being able to achieve sulfur conversions that are much higher than those by solvents in TGTUs. The proposed SRP system is optimized to achieve ~100% sulfur recovery (sub-ppmv) and has a substantially lower net present value (NPV) of 7.66 $/ton of sulfur processed compared to the cost of 18.65 $/ton for the SCOT process (Figure 4a and Table S11). In contrast, the SCOT process can reduce sulfur emissions only down to 200 ppmv.[6] The simulation results clearly reveal the potential of the prepared sorbent in the SRP application, as it can reach a higher sulfur removal efficiency while maintaining a much lower cost compared to the SCOT process.

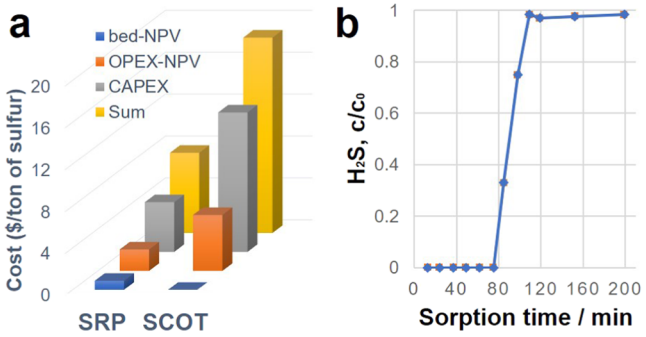

Figure 4. Economic analysis and performance in more complex, simulated Claus tail gas mixtures. (a) Economic comparison between the SRP and the SCOT processes based on sorbent 6:3:1 ($Cu_{6.2}Mg_{0.21}AlO_{7.9}$) (OPEX, operating expenditure; CAPEX, capital expenditure). The SRP process achieves a net present value (NPV) of 7.66 $/ton of sulfur, here indicated as "Sum", much lower than that using the SCOT process (18.65 $/ton of sulfur). Details of the comparison and cost breakdown are summarized in Table S11. (b) H_2S breakthrough curve of 6:3:1 ($Cu_{6.2}Mg_{0.21}AlO_{7.9}$) in simulated Claus tail gas mixture, with a sulfur capacity of 7.3 mmol/g.

In natural gas plants, the tail gas of the Claus process contains other components besides H_2S and the carrier gas, such as H_2O, CO_2, CO, H_2, and typically a few ppmv of hydrocarbons. To evaluate the performance of the sorbent under practical conditions, we carried out H_2S sorption using a gas mixture with a similar composition as the Claus process tail gas. As shown in Figure 4b, the breakthrough capacity (7.3 mmol/g) was also high in this mixed gas, clearly demonstrating that the sorbent works well under industrial conditions.

3.6. Why Does the MMO Sorbent 6:3:1 ($Cu_{6.2}Mg_{0.21}AlO_{7.9}$) Perform the Best? For CuO-based sorbents containing both Al_2O_3 and small fractions of MgO as additives, namely, 6:3:1 ($Cu_{6.2}Mg_{0.21}AlO_{7.9}$), 6.5:3:1 ($Cu_{6.9}Mg_{0.41}AlO_{8.8}$), and 5:3:1 ($Cu_{5.3}Mg_{0.47}AlO_{6.9}$), excessive SO_2 formation did not occur during cycling. However, the sulfur capacities and long-term stabilities of these sorbents are different, with 6:3:1 ($Cu_{6.2}Mg_{0.21}AlO_{7.9}$) outperforming 6.5:3:1 ($Cu_{6.9}Mg_{0.41}AlO_{8.8}$) and 5:3:1 ($Cu_{5.3}Mg_{0.47}AlO_{6.9}$) (Figure 5a). We propose that the catalytic amount of MgO additive in 6:3:1 ($Cu_{6.2}Mg_{0.21}AlO_{7.9}$) is dispersed by Al_2O_3 so that $MgSO_4$ is not formed during regeneration and does not interfere with CuO during the next sulfidation.

As shown in Figure 5b, crystalline $MgSO_4$ appeared in the XRD of the used sorbents 5:3:1 ($Cu_{5.3}Mg_{0.47}AlO_{6.9}$) and 6.5:3:1 ($Cu_{6.9}Mg_{0.41}AlO_{8.8}$), suggesting that even though CuS was fully converted to CuO after regeneration, sulfur species were still present. Elemental mapping of sorbent 6.5:3:1 after cycling revealed particles with high S content (~15.4 at. %), coinciding with a high concentration of Mg (~12.4 at. %) (Figure S29), likely originating from the $MgSO_4$ detected by XRD. On the other hand, in 6:3:1 ($Cu_{6.2}Mg_{0.21}AlO_{7.9}$) after cycling, the S concentration was very low (<0.43 at. %) (Figure S30) and no $MgSO_4$ peaks were observed in the XRD pattern (Figure 1e). In addition, impurity phases such as $MgSO_4$ and $Cu_3(SO_4)(OH)_4$ were observed in 5:3:1 ($Cu_{5.3}Mg_{0.47}AlO_{6.9}$) after the fourth sulfidation and 6.5:3:1 ($Cu_{6.9}Mg_{0.41}AlO_{8.8}$) after the fifth sulfidation, while 6:3:1 ($Cu_{6.2}Mg_{0.21}AlO_{7.9}$) after the tenth sulfidation contained the least amount of impurities, with CuS and some unreacted CuO as the predominant crystalline phases (Figure S31). Both the XRD and elemental mappings confirm that 6:3:1 ($Cu_{6.2}Mg_{0.21}AlO_{7.9}$) is the optimal composition for our sorbents that can be completely regenerated at 600 °C during cycling, leading to its high stability and regenerability.

The differences between sorbents 5:3:1 ($Cu_{5.3}Mg_{0.47}AlO_{6.9}$), 6:3:1 ($Cu_{6.2}Mg_{0.21}AlO_{7.9}$), and 6.5:3:1 ($Cu_{6.9}Mg_{0.41}AlO_{8.8}$) originate from their syntheses. The obtained MMOs after coprecipitation and calcination have different compositions compared to the original mixed metal nitrate solutions. The Mg content was significantly lower in the products than in the precursor nitrate solutions, which indicates that most Mg^{2+} was not precipitated during the synthesis. This phenomenon has been confirmed by several previous studies, as Mg^{2+} can only be completely precipitated when pH > 10.[27,28] The much lower concentration of Mg in sorbent 6:3:1 ($Cu_{6.2}Mg_{0.21}AlO_{7.9}$) compared to 5:3:1 ($Cu_{5.3}Mg_{0.47}AlO_{6.9}$) and 6.5:3:1 ($Cu_{6.9}Mg_{0.41}AlO_{8.8}$) is the major difference between these similarly synthesized materials. As shown in Figure 5c–e, sorbent 6:3:1 ($Cu_{6.2}Mg_{0.21}AlO_{7.9}$) has a much higher S/Cu ratio compared to 6.5:3:1 ($Cu_{6.9}Mg_{0.41}AlO_{8.8}$) after sulfidation, indicative of a higher conversion from CuO to CuS aided by the catalytic role of MgO, which is present in the former sorbent but absent in the latter due to the persistence of $MgSO_4$.

4. CONCLUSIONS

We developed methods for preparing solid sorbents containing Cu, Mg, and Al MMOs through a coprecipitation approach. Starting from the optimized mixed nitrate solutions with a Cu/Mg/Al = 6:3:1 composition, the obtained MMO 6:3:1 ($Cu_{6.2}Mg_{0.21}AlO_{7.9}$) demonstrated a stable, high sulfur capacity of ~7.5 mmol/g under 100 ppmv H_2S in N_2 for 10 successive sulfidation–regeneration cycles at 150 °C. After the sorbent was sulfidated, it could be regenerated with 5% O_2 in N_2 at 600 °C for 6 h to oxidize CuS back to CuO and restore the sorption activity.

For the optimal sorbent 6:3:1 ($Cu_{6.2}Mg_{0.21}AlO_{7.9}$), a small amount of dispersed MgO is suggested to be its distinguishing characteristic. By facilitating dissociation of H_2S, the MgO enables the high capacity of the MMO sorbent. With a higher MgO content, $MgSO_4$ is formed during cycling and cannot be

https://doi.org/10.1021/acs.iecr.1c02715
Ind. Eng. Chem. Res. 2021, 60, 14779–14787

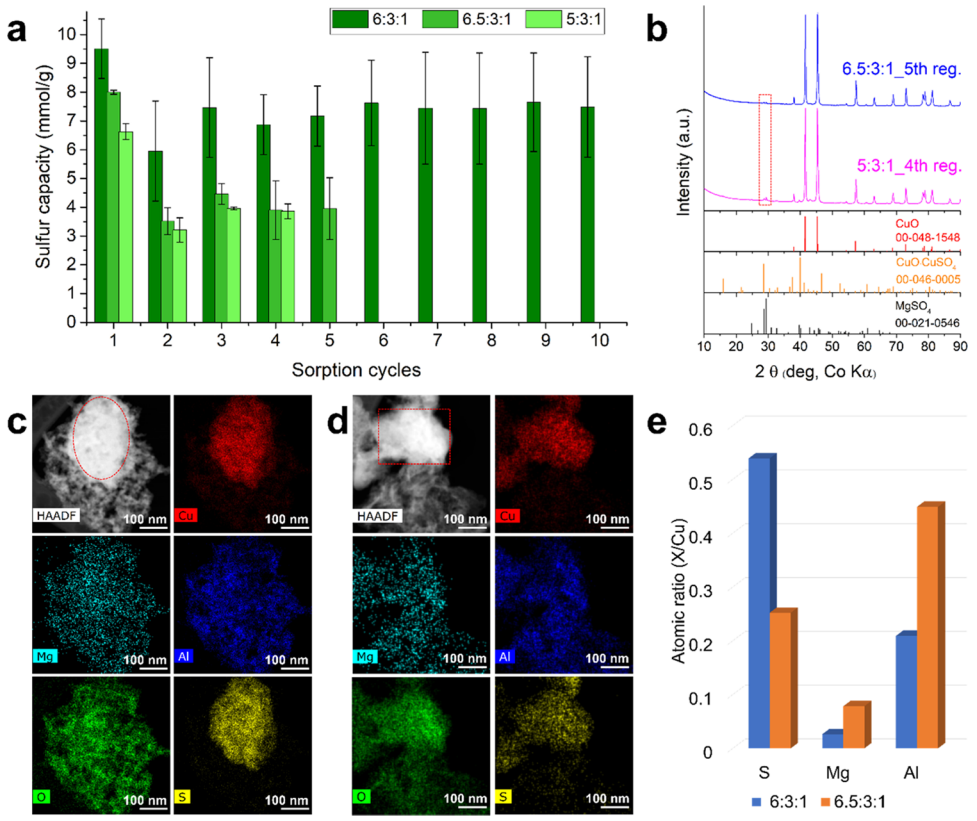

Figure 5. Influence of material composition on performance and structure. (a) Sulfur capacities of sorbents 6:3:1 ($Cu_{6.2}Mg_{0.21}AlO_{7.9}$), 6.5:3:1 ($Cu_{6.9}Mg_{0.41}AlO_{8.8}$), and 5:3:1 ($Cu_{5.3}Mg_{0.47}AlO_{6.9}$) over multiple cycles. Error bars are estimated from two separate samples prepared from two different batches. (b) XRD patterns of 5:3:1 ($Cu_{5.3}Mg_{0.47}AlO_{6.9}$) after four cycles and 6.5:3:1 ($Cu_{6.9}Mg_{0.41}AlO_{8.8}$) after five cycles; $MgSO_4$ diffraction peaks are highlighted in the box. HAADF-STEM image with the corresponding STEM-EDX elemental maps of (c) 6:3:1 ($Cu_{6.2}Mg_{0.21}AlO_{7.9}$) after the tenth sulfidation, and (d) 6.5:3:1 ($Cu_{6.9}Mg_{0.41}AlO_{8.8}$) after the fifth sulfidation. The compositions of particles from 6:3:1 ($Cu_{6.2}Mg_{0.21}AlO_{7.9}$) and 6.5:3:1 ($Cu_{6.9}Mg_{0.41}AlO_{8.8}$) marked in red in (c, d) are shown in (e), where X corresponds to S, Mg, and Al, respectively.

converted back to MgO during regeneration. Al_2O_3 helps disperse MgO and improve sorbent regenerability. Process assessment indicates that a sorption-based process can be superior to a commonly used commercial process.

■ ASSOCIATED CONTENT

Supporting Information

The Supporting Information is available free of charge at https://pubs.acs.org/doi/10.1021/acs.iecr.1c02715.

Additional experimental details; breakthrough data; XRD patterns; TEM micrographs; N_2 sorption data; comparison to other sorbents; and process-scale assessment (PDF)

■ AUTHOR INFORMATION

Corresponding Authors

K. Andre Mkhoyan − *Department of Chemical Engineering and Materials Science, University of Minnesota, Minneapolis, Minnesota 55455, United States;* orcid.org/0000-0003-3568-5452; Email: mkhoyan@umn.edu

Yasser Al Wahedi − *Department of Chemical Engineering, Khalifa University of Science and Technology, Abu Dhabi 2533, United Arab Emirates; Center for Catalysis and Separations, Khalifa University, Abu Dhabi 127788, United Arab Emirates;* Email: yasser.alwahedi@ku.ac.ae

Michael Tsapatsis − *Department of Chemical Engineering and Materials Science, University of Minnesota, Minneapolis, Minnesota 55455, United States; Department of Chemical and Biomolecular Engineering & Institute for NanoBioTechnology, Johns Hopkins University, Baltimore, Maryland 21218, United States; Applied Physics Laboratory, Johns Hopkins University, Laurel, Maryland 20723, United States;* orcid.org/0000-0001-5610-3525; Email: tsapatsis@jhu.edu

Andreas Stein − *Department of Chemistry, University of Minnesota, Minneapolis, Minnesota 55455, United States;* orcid.org/0000-0001-8576-0727; Email: a-stein@umn.edu

Authors

Wenyang Zhao − *Department of Chemistry, University of Minnesota, Minneapolis, Minnesota 55455, United States;* orcid.org/0000-0002-0828-3813

Balasubramanian Veerappan Vaithilingam − *Department of Chemical Engineering and Materials Science, University of Minnesota, Minneapolis, Minnesota 55455, United States; Department of Chemical Engineering, Khalifa University of Science and Technology, Abu Dhabi 2533, United Arab Emirates*

Supriya Ghosh − *Department of Chemical Engineering and Materials Science, University of Minnesota, Minneapolis, Minnesota 55455, United States*

https://doi.org/10.1021/acs.iecr.1c02715
Ind. Eng. Chem. Res. 2021, 60, 14779−14787

Xinyu Li − *Department of Chemical Engineering and Materials Science, University of Minnesota, Minneapolis, Minnesota 55455, United States*
Frank Geuzebroek − *Department of Research & Technology, Abu Dhabi Gas Industries Ltd. (GASCO), Abu Dhabi, Abu Dhabi 665, United Arab Emirates*
Adel Saif El Nasr − *Department of Research & Technology, Abu Dhabi Gas Industries Ltd. (GASCO), Abu Dhabi, Abu Dhabi 665, United Arab Emirates*
Ibrahim Khan − *Department of Research & Technology, Abu Dhabi Gas Industries Ltd. (GASCO), Abu Dhabi, Abu Dhabi 665, United Arab Emirates*
Satyadileep Dara − *Department of Chemical Engineering, Khalifa University of Science and Technology, Abu Dhabi 2533, United Arab Emirates*
Nitish Mittal − *Department of Chemical Engineering and Materials Science, University of Minnesota, Minneapolis, Minnesota 55455, United States*
Prodromos Daoutidis − *Department of Chemical Engineering and Materials Science, University of Minnesota, Minneapolis, Minnesota 55455, United States;* orcid.org/0000-0003-4803-0404
Saleh Al Hashimi − *SystemTrio Electronics LLC, Abu Dhabi 5588, United Arab Emirates*

Complete contact information is available at: https://pubs.acs.org/10.1021/acs.iecr.1c02715

Author Contributions

W.Z., B.V.V., and S.G. contributed equally to this work. A.S., M.T., and Y.A.W. conceived the project and designed the experiments, W.Z., B.V.V., and X.L. were responsible for material synthesis, data collection, and analysis. K.A.M. and S.G. were responsible for HAADF-STEM images and STEM-EDX elemental maps. Y.A.W., P.D., F.G., A.S.E.N., I.K., S.D., S.A.H., and N.M. were responsible for simulation studies. A.S., M.T., Y.A.W., and W.Z. wrote the manuscript. All authors contributed to the discussion and preparation of the manuscript and the Supporting Information.

Notes

The authors declare no competing financial interest.

■ ACKNOWLEDGMENTS

This project was financially supported by the Gas Sub-Committee R&D arm of Abu Dhabi National Oil Company, United Arab Emirates. Y.A.W. acknowledges financial support from a Khalifa University of Science and Technology Center for Catalysis and Separations grant under RCII-2018-024. S.G. and K.A.M. were supported by the National Science Foundation (NSF) through the UMN MRSEC under Award DMR-2011401. Parts of this work were carried out in the Characterization Facility, University of Minnesota, which receives partial support from the NSF through the MRSEC (Award Number DMR-2011401) and the NNCI (Award Number ECCS-2025124) programs. The authors thank Professor R. Lee Penn for use of the powder X-ray diffractometer.

■ REFERENCES

(1) Shah, M. S.; Tsapatsis, M.; Siepmann, J. I. Hydrogen sulfide capture: from absorption in polar liquids to oxide, zeolite, and metal-organic framework adsorbents and membranes. *Chem. Rev.* **2017**, *117*, 9755−9803.
(2) Peluso, A.; Gargiulo, N.; Aprea, P.; Pepe, F.; Caputo, D. Nanoporous materials as H_2S adsorbents for biogas purification: a review. *Sep. Purif. Rev.* **2019**, *48*, 78−89.
(3) Habeeb, O. A.; Kanthasamy, R.; Ali, G. A. M.; Sethupathi, S.; Yunus, R. B. M. Hydrogen sulfide emission sources, regulations, and removal techniques: a review. *Rev. Chem. Eng.* **2018**, *34*, 837−854.
(4) Kohl, A. L.; Nielsen, R. *Gas Purification*; Elsevier, 1997.
(5) Gary, J. H.; Handwerk, G. E.; Kaiser, M. J.; Geddes, D. *Petroleum Refining: Technology and Economics*; CRC Press, 2007.
(6) Miller, L. N.; Macriss, R. A.; Zawacki, T. S. Process for Acid Gas Removal from Gaseous Mixtures. U.S. Patent US4,080,424, 1978.
(7) Eow, J. S. Recovery of sulfur from sour acid gas: A review of the technology. *Environ. Prog.* **2002**, *21*, 143−162.
(8) Swaim, C. D. The Shell Claus Offgas Treating (SCOT) Process. In *Sulfur Removal and Recovery from Industrial Processes*; Pfeiffer, J. B., Ed.; Advances in Chemistry Series; American Chemical Society, 1975; Vol. *139*, pp 111−119.
(9) Al Wahedi, Y.; Torres, A. I.; Al Hashimi, S.; Dowling, N. I.; Daoutidis, P.; Tsapatsis, M. Economic assessment of temperature swing adsorption systems as Claus tail gas clean up units. *Chem. Eng. Sci.* **2015**, *126*, 186−195.
(10) Bagreev, A.; Bandosz, T. J. Study of hydrogen sulfide adsorption on activated carbons using inverse gas chromatography at infinite dilution. *J. Phys. Chem. B* **2000**, *104*, 8841−8847.
(11) Bagreev, A.; Rahman, H.; Bandosz, T. J. Study of H_2S adsorption and water regeneration of spent coconut-based activated carbon. *Environ. Sci. Technol.* **2000**, *34*, 4587−4592.
(12) Elyassi, B.; Wahedi, Y. A.; Rajabbeigi, N.; Kumar, P.; Jeong, J. S.; Zhang, X.; Kumar, P.; Balasubramanian, V. V.; Katsiotis, M. S.; Andre Mkhoyan, K.; Boukos, N.; Hashimi, S. A.; Tsapatsis, M. A high-performance adsorbent for hydrogen sulfide removal. *Microporous Mesoporous Mater.* **2014**, *190*, 152−155.
(13) Dhage, P.; Samokhvalov, A.; Repala, D.; Duin, E. C.; Bowman, M.; Tatarchuk, B. J. Copper-promoted ZnO/SiO_2 regenerable sorbents for the room temperature removal of H_2S from reformate gas streams. *Ind. Eng. Chem. Res.* **2010**, *49*, 8388−8396.
(14) Vamvuka, D.; Arvanitidis, C.; Zachariadis, D. Flue gas desulfurization at high temperatures: A review. *Environ. Eng. Sci.* **2004**, *21*, 525−548.
(15) Elseviers, W. F.; Verelst, H. Transition metal oxides for hot gas desulphurisation. *Fuel* **1999**, *78*, 601−612.
(16) Khabazipour, M.; Anbia, M. Removal of hydrogen sulfide from gas streams using porous materials: A review. *Ind. Eng. Chem. Res.* **2019**, *58*, 22133−22164.
(17) Xue, M.; Chitrakar, R.; Sakane, K.; Ooi, K. Screening of adsorbents for removal of H_2S at room temperature. *Green Chem.* **2003**, *5*, 529−534.
(18) Bakker, W. J. W.; Kapteijn, F.; Moulijn, J. A. A high capacity manganese-based sorbent for regenerative high temperature desulfurization with direct sulfur production. *Chem. Eng. J.* **2003**, *96*, 223−235.
(19) Liu, D.; Chen, S.; Fei, X.; Huang, C.; Zhang, Y. Regenerable CuO-based adsorbents for low temperature desulfurization application. *Ind. Eng. Chem. Res.* **2015**, *54*, 3556−3562.
(20) Abbasian, J.; Slimane, R. B. A regenerable copper-based sorbent for H_2S removal from coal gases. *Ind. Eng. Chem. Res.* **1998**, *37*, 2775−2782.
(21) Yasyerli, S.; Dogu, G.; Ar, I.; Dogu, T. Activities of copper oxide and Cu−V and Cu−Mo mixed oxides for H_2S removal in the presence and absence of hydrogen and predictions of a deactivation model. *Ind. Eng. Chem. Res.* **2001**, *40*, 5206−5214.
(22) Yasyerli, S.; Dogu, G.; Ar, I.; Dogu, T. Activities of copper oxide and Cu−V and Cu−Mo mixed oxides for H_2S removal in the presence and absence of hydrogen and predictions of a deactivation model. *Ind. Eng. Chem. Res.* **2001**, *40*, 5206−5214.
(23) Dunn, J. G.; Muzenda, C. Thermal oxidation of covellite (CuS). *Thermochim. Acta* **2001**, *369*, 117−123.

(24) Kyotani, T.; Kawashima, H.; Tomita, A.; Palmer, A.; Furimsky, E. Removal of H_2S from hot gas in the presence of Cu-containing sorbents. *Fuel* **1989**, *68*, 74−79.
(25) Rodriguez, J. A.; Maiti, A. Adsorption and decomposition of H_2S on MgO(100), NiMgO(100), and ZnO(0001) surfaces: A first-principles density functional study. *J. Phys. Chem. B* **2000**, *104*, 3630−3638.
(26) Rodriguez, J. A.; Jirsak, T.; Chaturvedi, S. Reaction of H_2S with MgO(100) and Cu/MgO(100) surfaces: Band-gap size and chemical reactivity. *J. Chem. Phys.* **1999**, *111*, 8077−8087.
(27) Wang, Q.; Tay, H. H.; Guo, Z.; Chen, L.; Liu, Y.; Chang, J.; Zhong, Z.; Luo, J.; Borgna, A. Morphology and composition controllable synthesis of Mg−Al−CO_3 hydrotalcites by tuning the synthesis pH and the CO_2 capture capacity. *Appl. Clay Sci.* **2012**, *55*, 18−26.
(28) Seron, A.; Delorme, F. Synthesis of layered double hydroxides (LDHs) with varying pH: A valuable contribution to the study of Mg/Al LDH formation mechanism. *J. Phys. Chem. Solids* **2008**, *69*, 1088−1090.
(29) Schneider, W. F.; Li, J.; Hass, K. C. Combined computational and experimental investigation of SO_x adsorption on MgO. *J. Phys. Chem. B* **2001**, *105*, 6972−6979.
(30) Thibault, J. D.; Steward, F. R.; Ruthven, D. M. The kinetics of absorption of SO_3 in calcium and magnesium oxides. *Can. J. Chem. Eng.* **1982**, *60*, 796−801.
(31) Scheidema, M. N.; Taskinen, P. Decomposition thermodynamics of magnesium sulfate. *Ind. Eng. Chem. Res.* **2011**, *50*, 9550−9556.
(32) Al Wahedi, Y.; Rabie, A. H.; Al Shaiba, A.; Geuzebroek, F.; Daoutidis, P. Optimization of adsorption-based natural gas dryers. *Ind. Eng. Chem. Res.* **2016**, *55*, 4658−4667.

https://doi.org/10.1021/acs.iecr.1c02715
Ind. Eng. Chem. Res. 2021, 60, 14779−14787